Optics Letters

Evolution of the nonlinear Raman–Nath diffraction from near field to far field

Dongmei Liu,[1] Dunzhao Wei,[2] Min Gu,[1,*] Yong Zhang,[2,4] Xiaopeng Hu,[2] Min Xiao,[2,3] and Peng Han[1]

[1]School of Physics and Telecommunication Engineering, South China Normal University, Guangzhou 510006, China
[2]National Laboratory of Solid State Microstructures, Nanjing University, Nanjing 210093, China
[3]Department of Physics, University of Arkansas, Fayetteville, Arkansas 72701, USA
[4]e-mail: zhangyong@nju.edu.cn
*Corresponding author: mingu@m.scnu.edu.cn

Received 7 May 2018; accepted 26 May 2018; posted 7 June 2018 (Doc. ID 331030); published 28 June 2018

In this Letter, we studied the near-field effect of the nonlinear Raman–Nath diffraction experimentally in a 1D periodically poled $LiTaO_3$ crystal and established a theoretical relationship between the nonlinear effect in the near field and the corresponding effect in the far field. The interference of far-field spots in the near field constitutes the nonlinear Talbot self-imaging effect. Our results not only enhance our understanding of the nonlinear Talbot effect, but they also indicate potential applications of this effect in domain inspection and domain design.

OCIS codes: (070.6760) Talbot and self-imaging effects; (190.2620) Harmonic generation and mixing.

https://doi.org/10.1364/OL.43.003168

Nonlinear photonic crystals (NPCs) [1,2], with their periodic modulation of the second-order susceptibility $\chi^{(2)}$, have been widely studied for use in nonlinear frequency conversion because they could provide an abundance of reciprocal vectors to compensate for the phase mismatch that occurs during the nonlinear interaction process, that is, the quasi-phase-matching (QPM) process [3–5]. In addition to assisting with the QPM process, the spatial phase modulation capabilities of NPCs have been also used to modulate second-harmonic (SH) wavefronts in one dimension for the generation of special beams, including Airy beams and Hermite–Gaussian beams [6–10]. Both the efficient nonlinear frequency conversion and 1D phase modulation procedures are based on collinear wave mixing. Various other interesting phenomena are also generated using noncollinear wave-mixing processes in NPCs, including the nonlinear Bragg diffraction [11], nonlinear Raman–Nath (RN) diffraction, and nonlinear Čerenkov diffraction [12].

In the noncollinear nonlinear wave-mixing process, the phase mismatch can be divided into two components: a transverse component and a longitudinal component. The nonlinear Bragg diffraction effect occurs when both components are compensated to satisfy the noncollinear QPM process, which has previously been used to generate multiple SH spots and Bessel beams [13–15]. If only the longitudinal phase mismatch is compensated, it can be considered to be the nonlinear Čerenkov diffraction phenomenon [16–18]. Therefore, the phenomenon where only the transverse phase-matched components are compensated is automatically called nonlinear RN diffraction. The RN diffraction effect was first reported by Saltiel *et al.*, used to generate the SH Bessel beams [19] and expanded to engineering of a 2D SH field by superposing nonlinear susceptibility modulations or structuring fundamental waves [20–23]. The resulting engineered 2D SH fields have been used to demonstrate nonlinear imaging [24–26], superfocusing [27], and a diffraction-free array beam [28]. However, most previous studies on nonlinear RN diffraction in NPCs have essentially focused on far-field characteristics; to date, the near-field characteristics of this process have not been investigated sufficiently, and there is a particular interest in the relationship between the nonlinear RN diffraction far-field patterns and the near-field effect.

In this Letter, we present an experimental study of the near-field and far-field effects of the SH waves generated using a 1D periodically poled $LiTaO_3$ (PPLT) crystal. The far-field effect is shown as the RN diffraction, while the near-field effect is the previously reported nonlinear Talbot effect [24,25]. Theoretical and numerical calculations are performed to establish the relationship between the nonlinear near-field effect and the far-field nonlinear RN diffraction. Our results show that the nonlinear Talbot effect can also be understood as the interference of far-field patterns in the near field, which greatly enriches the concept of nonlinear Talbot self-images.

In the experiments, we used a Z-cut periodically poled $LiTaO_3$ sample with dimensions of 10 mm(x) × 1.2 mm(y) × 0.5 mm(z) [Fig. 1(a)], which was fabricated using an electric-field poling technique at room temperature with a poling period $\Lambda = 29.6$ μm and a duty cycle of $D \sim 67\%$. A femtosecond mode-locked Ti:sapphire laser operating at a wavelength of 920 nm was used to provide the fundamental input field. The pulse width was ~75 fs with a repetition rate of 80 MHz. The laser beam was loosely focused using a 300-mm focal length lens and then directed into a 1D PPLT crystal along the y axis with its polarization parallel to the z axis,

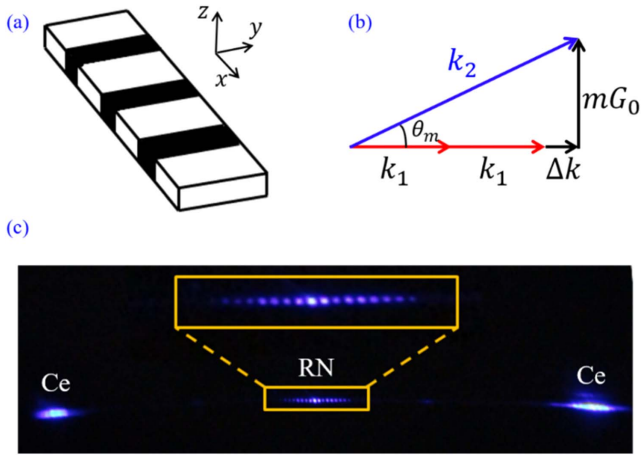

Fig. 1. (a) Design of the 1D nonlinear photonic structure, (b) the phase-matching diagram, (c) and the second-harmonic pattern observed on the screen (inset: expanded view of the nonlinear Raman–Nath diffraction). The peripheral spots correspond to the nonlinear Čerenkov diffraction (marked Če), while the central spots are from the nonlinear Raman–Nath diffraction (marked RN).

thereby using the largest nonlinear-optical coefficient (d33) of the $LiTaO_3$ crystal [Fig. 1(a)]. The phase-matching diagram shown in Fig. 1(b) combines the wave vectors k_1 and k_2, which correspond to the beam's fundamental frequency and its SH, respectively. The transverse component $k_2 \sin\theta_m = mG_0$ of the phase matching determines the different diffraction angles θ_m, where m is the nonlinear RN diffraction order, and $G_0 = \frac{2\pi}{\Lambda}$ is the primary reciprocal lattice vector. The SH pattern [Fig. 1(c)] is observed on a screen located 4 cm away from the center of the sample. Adjacent to the side spots that correspond to nonlinear Čerenkov diffraction, it is possible to distinguish a set of ordered SH spots near the passed fundamental beam. These SH beams are believed to correspond to the nonlinear RN diffraction because of the periodicity of the structure in the transverse direction. In the far field, we can clearly observe 15 SH beams that correspond to the seven orders [see the enlargement in Fig. 1(c)].

Under the undepleted pump approximation, the spectral intensity of the SH field in a 1D PPLT crystal can be written as a function of the spatial frequency K_x and the propagation length L_y of the fundamental wave in the crystal [29,30]:

$$I_2(K_x, L_y) = \pi a^2 L_y^2 \beta_2^2 I_1^2 \times \{\mathrm{sinc}[L_y(\Delta k - K_x^2/2k_2)/2]\}^2 \times \left\{\sum_{m=0,\pm1,\pm2,\ldots} g_m \exp[-a^2(mG_0 + K_x)^2/8]\right\}^2, \quad (1)$$

where a is the beam width of the fundamental wave, and $\beta_2 = k_2\chi^{(2)}/(2n_{e2}^2)$ is the nonlinear coupling coefficient, where n_{e2} is the refractive index at the SH frequency. We assume that the fundamental wave is a Gaussian beam of the equation $E_1(x) = E_{10}e^{-x^2/a^2}$, so $I_1 = E_1^2$. In addition, $\Delta k = k_2 - 2k_1$ is the wave vector mismatch between the fundamental and SH waves. The Fourier coefficients are $g_m = 2D - 1 (m = 0)$ and $g_m = 2\sin(\pi mD)/(\pi m)(m \neq 0)$, and D is the duty cycle of the 1D PPLT crystal.

To observe the near-field nonlinear effect, we used a 100× objective lens with a numerical aperture (NA) of 0.7, moving along the y axis near the back of the sample; the movements of the lens were controlled using a precision translation stage. The input pump power was set at 66 mW. The generated SH pattern was then projected onto a charge-coupled device (CCD) camera, which moved jointly with the objective lens. The step was set to 0.5 μm. The intensity distributions along the x direction in the recorded images compose the "carpet" in Fig. 2(a). The measured evolution of the SH carpet within the range $y = 2000$ μm [Fig. 2(a)] clearly highlights the imaging performance. We find this pattern to be similar to the carpet produced by nonlinear Talbot self-imaging. Experimentally, in comparison to the initial pattern at $y = 0$ μm, the SH pattern at $y = 1900$ μm presents a half-period shift along the x direction, which results from the π-phase shift of the generated SH field [31]. That is, all bright SH stripes in the output face of the object evolve into dark stripes, and vice versa. The period of the image is equal to the period of the sample. We verified that the self-image of the 1D PPLT crystal occurs at $y = 1900$ μm and that the imaging performance is similar to that of half of the self-imaging length. At smaller propagation lengths, sub-images can also be observed. For example, at $y = 910$ μm, the image is half the original size and appears with half the period of the sample, thus corresponding to one-quarter of the Talbot self-imaging length. We note that the features at the other observation planes are also correlated with the characteristics of the Talbot self-imaging effect. The experimental setup (which is not shown here) is the same as that used in our previous studies of the SH Talbot effect.

After careful measurements, the characteristic SH field patterns were recorded at different observation planes (Fig. 3) to represent a variety of "photonic carpets" within the Fresnel diffraction region. The diffraction patterns change considerably [Figs. 3(a)–3(f)] as the images are acquired at increasing distances away from the crystal. For example, the periods of the SH patterns increase, while their intensities decrease. The half-Talbot self-imaging plane was observed at $y = 1900$ μm [Fig. 3(f)], which is consistent with the theoretically calculated

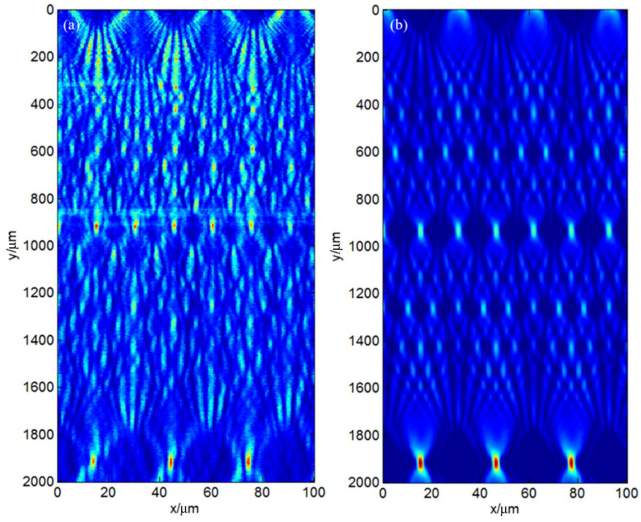

Fig. 2. (a) Talbot "carpets" along the propagation direction obtained from experiments, and (b) numerical results obtained from the nonlinear RN diffraction with the inverse method.

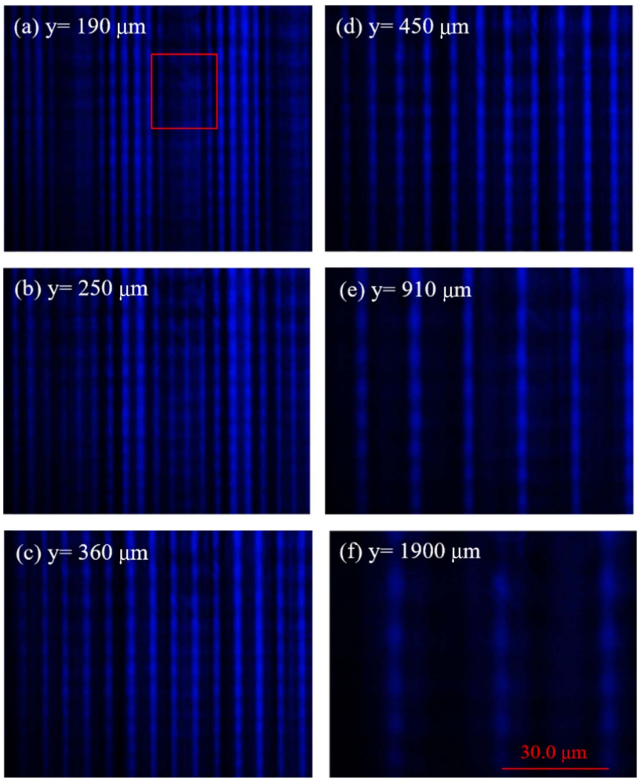

Fig. 3. Images of the SH patterns recorded using a conventional optical microscope at different Talbot planes. The images were all formed within the half-Talbot length. The SH patterns correspond to the Talbot lengths of (a) 1/20, (b) 1/15, (c) 1/11, (d) 1/8, (e) 1/4, and (f) 1/2.

SH half-Talbot length of $Y_T/2 = 2\Lambda^2/\lambda = 1905$ μm, where λ is the wavelength of the fundamental beam, and Λ is the period of the PPLT. The small deviation may be the result of translation-stage hysteresis. At the half Talbot plane, the period of the interference pattern is 29.7 μm, which is consistent with the sample period of 29.6 μm. In the other fractional Talbot planes, complex diffraction patterns that result from the Fresnel diffraction interference of the SH waves can be seen. Near the end face of the sample [Fig. 3(a)], the SH pattern at $y = 190$ μm has a nonuniform period. The intensity is at its highest here, and some detailed structures can be observed in the image [see the area marked in Fig. 3(a)]. This occurs because the higher-order diffraction fields near the output surface of the sample are recorded in their entirety by the CCD. We also determined from the experiments that the periods of the patterns increase [Figs. 3(b)–3(f)] and that the qualities of the image after the half Talbot plane worsen when compared with those at other fractional planes. The images from the experiment, which are shown in Figs. 3(b)–3(f), yield the SH pattern periods of 4.3 μm, 6.0 μm, 7.5 μm, 14.5 μm, and 29.7 μm at the Talbot lengths of 1/15, 1/11, 1/8, 1/4, and 1/2, respectively. These periods correspond to the predicted periods given by $\Lambda' = 2\Lambda * \frac{p}{q}$, where p and q are prime numbers, for self-images to occur at the different planes in a 1D PPLT.

To verify the theory that the nonlinear Talbot self-imaging effect is indeed formed by the near-field effect of the nonlinear RN diffraction, we performed numerical simulations using the inverse method. First, we extracted the relative intensities of the far-field spots from the nonlinear RN diffraction pattern [Fig. 1(c)] and used A_m to represent the relative intensities of different order m, with values including $A_0 = 1$, $A_1 = 0.6424$, $A_{-1} = 0.6303$, $A_2 = 0.4303$, $A_{-2} = 0.4182$, $A_3 = 0.4424$, $A_{-3} = 0.4970$, $A_4 = 0.3879$, $A_{-4} = 0.5576$, $A_5 = 0.3455$, $A_{-5} = 0.4303$, $A_6 = 0.2121$, $A_{-6} = 0.3212$, $A_7 = 0.1333$, and $A_{-7} = 0.1879$, which are all in agreement with the values obtained from theoretical calculations using Eq. (1). In addition, measurement of the first-order diffraction angle in the experiment gives $\theta_1 = 0.0151$ rad. Second, in the simulation, each spot can be considered to be a Gaussian beam with a wavelength of 460 nm. Third, using the multiple-beam interference, all spots mutually interfere, and this results in an SH propagation carpet [see Fig. 2(b)]. For the image shown in Fig. 2(a), the simulation reproduces almost the same pattern, as depicted in Fig. 2(b), using the experimental parameters, which indicates good agreement with the experimental data. Based on Fig. 2(b), the numerical simulation confirms the nonlinear Talbot self-imaging behavior, and thus it verifies that the near-field effect of the nonlinear RN diffraction is indeed the nonlinear Talbot effect in a 1D PPLT crystal. This implies that the nonlinear Talbot effect studied here can also be interpreted to be the near-field interference of the far-field spots. To enable further examination of the observed near-field effect, we have theoretically demonstrated the evolution of the SH field [Fig. 4] in the 1D PPLT using the finite difference method [32]. The input pump laser was still operating at the 920 nm wavelength. For Fig. 4, the length of the crystal was 1200 μm along the y axis, and the SH wave propagation distance in the free-space is again 2000 μm. We found that in the Fresnel near field (from the output face of the crystal to 3200 μm), the Talbot effect was also observed, which validates the experimental results once more.

In addition, we also determined experimentally that the nonlinear Čerenkov diffraction affects the image quality. The intensity of the nonlinear Čerenkov diffraction is high [as shown in Fig. 1(c)] and is close to the nonlinear RN diffraction in the near field. Therefore, this diffraction can be partially collected using an objective lens with high NA. This is why we are able to find some detailed structures near the end surface of the sample in the experiments [Fig. 3(a)] when the pattern is nonuniform. As the propagation distance increases, the Čerenkov diffraction and the RN diffraction separate completely, meaning that the patterns only contain information about the nonlinear RN diffraction. Without the effects of the nonlinear Čerenkov diffraction, the SH image becomes much clearer in more distant fractional Talbot planes [see Figs. 3(c)–3(e)].

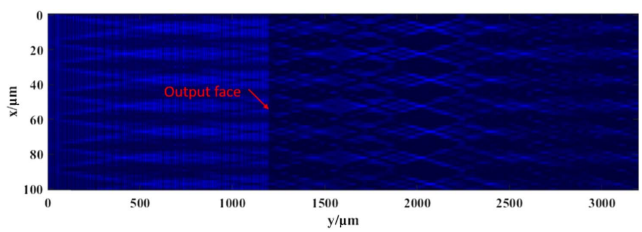

Fig. 4. Evolution of the field in the 1D PPLT crystal, as determined using the finite difference method. The length of the crystal is 1200 μm, and the propagation distance in the free-space is 2000 μm.

We note that no such analysis was implemented in previous nonlinear Talbot experiments.

Note that the focusing beam that was used in the experiment has a beam size of ~200 μm, which covers an area of approximately seven periods of the sample. The Talbot effect is well-known to be a near-field diffraction phenomenon from a periodic object. To ensure high-quality images over long distances, it is best to have as many periodic structures as possible participating in the self-imaging process. This raises an interesting question: How can we realize nonlinear Talbot self-imaging? It appears that the nonlinear RN diffraction provides sufficient diffraction orders at the end face of the sample that can effectively interfere with each other to generate the nonlinear Talbot effect.

In summary, we have demonstrated an evolutionary process from the near-field to the far-field nonlinear RN diffraction in an NPC. Going beyond the previously investigated nonlinear effect, this work has established a relationship between the nonlinear effect in the near field and that in the far field. In particular, our investigation indicates that the nonlinear Talbot effect can be understood to be the interference of far-field spots occurring in the near field. Furthermore, the nonlinear Čerenkov diffraction affects the quality of the SH imaging near the end face of the sample. By including these two factors, the results of the simulations of the multiple-beam interference agree well with the experimental results. Our results not only enrich the concept of the nonlinear Talbot self-imaging effect, but also open the door to a broader variety of applications of nonlinear RN diffraction in fields such as imaging, domain design, and domain inspection.

Funding. Natural Science Foundation of Jiangsu Province (BK20140590, BK20160636); National Natural Science Foundation of China (NSFC) (11404165); Open Fund of the National Lab of Solid State Microstructures (Nanjing University) (M30009); China Postdoctoral Science Foundation (2018M633064).

Acknowledgment. We thank the Physics Experiment Teaching Center of South China Normal University, the Optics Laboratory, for the use of their equipment.

REFERENCES

1. J. A. Armstrong, N. Bloembergen, J. Ducuing, and P. S. Pershan, Phys. Rev. **127**, 1918 (1962).
2. V. Berger, Phys. Rev. Lett. **81**, 4136 (1998).
3. M. M. Fejer, G. A. Magel, D. H. Jundt, and R. L. Byer, IEEE J. Quantum Electron. **28**, 2631 (1992).
4. S. Zhu, Y. Y. Zhu, and N. B. Ming, Science **278**, 843 (1997).
5. N. G. Broderick, G. W. Ross, H. L. Offerhaus, D. J. Richardson, and D. C. Hanna, Phys. Rev. Lett. **84**, 4345 (2000).
6. T. Ellenbogen, N. Voloch-Bloch, A. Ganany-Padowicz, and A. Arie, Nat. Photonics **3**, 395 (2009).
7. X. H. Hong, B. Yang, C. Zhang, Y. Q. Qin, and Y. Y. Zhu, Phys. Rev. Lett. **113**, 163902 (2014).
8. S. Trajtenberg-Mills, I. Juwiler, and A. Arie, Laser Photon. Rev. **9**, L40 (2015).
9. S. Trajtenberg-Mills, I. Juwiler, and A. Arie, Optica **4**, 153 (2017).
10. Y. Q. Qin, C. Zhang, Y. Y. Zhu, X. P. Hu, and G. Zhao, Phys. Rev. Lett. **100**, 063902 (2008).
11. I. Freund, Phys. Rev. Lett. **21**, 1404 (1968).
12. Y. Zhang, Z. D. Gao, Z. Qi, S. N. Zhu, and N. B. Ming, Phys. Rev. Lett. **100**, 163904 (2008).
13. X. Fang, D. Wei, D. Liu, W. Zhong, R. Ni, Z. Chen, X. Hu, Y. Zhang, S. N. Zhu, and M. Xiao, Appl. Phys. Lett. **107**, 161102 (2015).
14. S. M. Saltiel, D. N. Neshev, R. Fischer, W. Krolikowski, A. Arie, and Y. S. Kivshar, Phys. Rev. Lett. **100**, 103902 (2008).
15. N. G. R. Broderick, R. T. Bratfalean, T. M. Monro, D. J. Richardson, and C. M. de Sterke, J. Opt. Soc. Am. B **19**, 2263 (2002).
16. S. M. Saltiel, Y. Sheng, N. Voloch-Bloch, D. N. Neshev, W. Krolikowski, A. Arie, K. Koynov, and Y. S. Kivshar, IEEE J. Quantum Electron. **45**, 1465 (2009).
17. N. An, H. Ren, Y. Zheng, X. Deng, and X. Chen, Appl. Phys. Lett. **100**, 221103 (2012).
18. H. X. Li, S. Y. Mu, P. Xu, M. L. Zhong, C. D. Chen, X. P. Hu, W. N. Cui, and S. N. Zhu, Appl. Phys. Lett. **100**, 101101 (2012).
19. S. M. Saltiel, D. N. Neshev, R. Fischer, W. Krolikowski, A. Arie, and Y. S. Kivshar, Jpn. J. Appl. Phys. **47**, 6777 (2008).
20. Y. Chen, W. Dang, Y. Zheng, X. Chen, and X. Deng, Opt. Lett. **38**, 2298 (2013).
21. N. V. Bloch, K. Shemer, A. Shapira, R. Shiloh, I. Juwiler, and A. Arie, Phys. Rev. Lett. **108**, 233902 (2012).
22. A. Shapira, R. Shiloh, I. Juwiler, and A. Arie, Opt. Lett. **37**, 2136 (2012).
23. H. Liu, J. Li, X. Zhao, Y. Zheng, and X. Chen, Opt. Express **24**, 15666 (2016).
24. Y. Zhang, J. Wen, S. N. Zhu, and M. Xiao, Phys. Rev. Lett. **104**, 183901 (2010).
25. Z. Chen, D. Liu, Y. Zhang, J. Wen, S. N. Zhu, and M. Xiao, Opt. Lett. **37**, 689 (2012).
26. R. E. Lu, R. Z. Zhao, X. Feng, B. Yang, X. H. Hong, C. Zhang, Y. Q. Qin, and Y. Y. Zhu, Phys. Rev. Lett. **120**, 067601 (2018).
27. D. Liu, Y. Zhang, J. Wen, Z. Chen, D. Wei, X. Hu, G. Zhao, S. N. Zhu, and M. Xiao, Sci. Rep. **4**, 6134 (2014).
28. D. Liu, D. Wei, Y. Zhang, Z. Chen, R. Ni, B. Yang, X. Hu, Y. Q. Qin, S. N. Zhu, and M. Xiao, Sci. Rep. **7**, 40856 (2017).
29. Y. Sheng, Q. Kong, W. Wang, K. Kalinowski, and W. Krolikowski, J. Phys. B **45**, 055401 (2012).
30. A. M. Vyunishev, V. V. Slabko, I. S. Baturin, A. R. Akhmatkhanov, and V. Y. Shur, Opt. Lett. **39**, 4231 (2014).
31. J. Wen, Y. Zhang, and M. Xiao, Adv. Opt. Photon. **5**, 83 (2013).
32. M. Zhou, J. Ma, C. Zhang, and Y. Qin, Opt. Express **20**, 1261 (2012).